

THESIS

COMPARATIVE ANALYSIS OF $\text{Cu}(\text{InGa})\text{Se}_2$ SOLAR CELLS

Submitted by

Kahl Counts

Department of Physics

In partial fulfillment of the requirements

For the Degree of Master of Science

Colorado State University

Fort Collins, Colorado

Spring 2016

Masters Committee:

Advisor: James Sites

W. S. Sampath
Jose de la Venta

Copyright by Kahl Counts 2016

All Rights Reserved

ABSTRACT

COMPARATIVE ANALYSIS OF $\text{Cu}(\text{InGa})\text{Se}_2$ SOLAR CELLS

$\text{Cu}(\text{InGa})\text{Se}_2$, often abbreviated CIGS, photovoltaics have proven to be a commercially viable solar-energy conversion technology. Diverse processes have been employed in the manufacture, with varying end products, most resulting in high efficiency. A collaborative project was undertaken with several CIGS labs and industrial partners to explore the different electrical and spatial characteristics of CIGS solar cells relative to one another. Characterization methods utilized include, current-voltage measurements, quantum efficiency, capacitance-frequency and capacitance-voltage, electroluminescence, light-beam-induced current and Auger profiling. Specific parameters for each cell were extracted from the measurements. Together the methods used are a tool for understanding device performance and optimization. Efforts were made to identify strengths, similarities and differences and to connect processing details with observed characteristics.

ACKNOWLEDGMENTS

To begin, I would like to say that I am incredibly fortunate to have been part of the physics department at Colorado State University. I have never been part of a more amazing group of incredible, driven individuals. Though the experience has been arduous, it has made me much stronger. I can say I am a much better person for having been through this experience with such exceptional people.

Foremost among those individuals, I would like to thank Jim Sites. I am grateful for every opportunity you have made available to me, every piece of advice, and for building a lab and community of scientists committed to excellence.

Thanks to the other physics communities that helped me grow. The faculty at Fredonia State University, particularly Prof. Erica Simoson, and Prof. Justin Conroy, and from Jamestown Community College, the instructor who ignited my love for physics, Dr. Marie Plumb.

Thank you to everyone in the PV lab, Jennifer Drayton, Katherine Zaunbrecher, Russell Geisthardt, John Raguse, Tao Song, Andrew Moore, Alex Huss, Ramesh Pandey and W.S. Sampath.

Thank you to all my fellow students who worked beside me along the way, there are too many to name but particularly Chase Calvi and John Huihui.

Lastly and most importantly, thank you to Elise, for being my better half through the years and continuously making me want to be better. I cannot express how much your support has meant, and how much better this journey has been because of you.

TABLE OF CONTENTS

Abstract	ii
Acknowledgments	iii
Table of Contents	iv
List of Tables	v
List of Figures	vi
1 Solar Power	1
1.1 The Photovoltaic Effect	1
1.2 The Solar Boom	1
1.3 A Case for Thin-film photovoltaics	2
2 CIGS Solar Cell Technology	3
2.1 CIGS	3
2.2 Device Physics	4
2.3 Device Structure	6
2.4 CIGS Variations	8
3 Solar Cell Characterization	11
3.1 Current-Density vs. Voltage	11
3.2 Quantum Efficiency	14
3.3 Capacitance Measurements	16
3.4 Electroluminescence	18
3.5 Light-Beam-Induced Current	18
3.6 Scanning Electron Microscopy and Auger Profiling	19
4 Measurements and Analysis	20
4.1 J-V	20
4.2 QE and Reflection	23
4.3 Capacitance	25
4.4 Electroluminescence	27
4.5 LBIC	29
4.6 SEM	30
4.7 Auger	30
5 Summary	35
Bibliography	39

LIST OF TABLES

2.1	Participant processing details	8
4.1	J-V performance parameters	20
4.2	J_{SC} losses	24
4.3	Atomic concentrations	31

LIST OF FIGURES

2.1	Unit cell of the chalcopyrite lattice	3
2.2	p-n junction formation	4
2.3	CIGS band diagram	6
2.4	Stack diagram	7
3.1	Representative JV curve	12
3.2	Equivalent circuit diagram	13
3.3	QE curve from a CIGS cell w/ J_{SC} losses	15
3.4	Capacitance-frequency and A^2/C^2 vs Voltage of a CIGS cell	16
3.5	Hole density vs distance from junction	17
4.1	J-V under standard illumination.	21
4.2	J-V normalized to S-Q limit	22
4.3	Internal quantum efficiency.	23
4.4	A^2 / C^2 vs Voltage	25
4.5	Hole density vs distance from junction	26
4.6	Electroluminescence	27
4.7	EL vs. V_{OC}	28
4.8	LBIC	29
4.9	SEM cross-sections	30
4.10	Auger atomic profiles	32
4.11	E_g vs time	33
5.1	V_{OC} vs E_g	37

Chapter 1

SOLAR POWER

1.1 The Photovoltaic Effect

The photovoltaic effect is the process by which sunlight is converted into electrical energy. This occurs when a semiconducting material absorbs a photon's energy and generates an electron-hole pair. If the photon's energy is sufficiently large, the charge carriers will move to a higher energy state. Semiconducting materials arranged as a p-n junction collect these energetic charge carriers and facilitate their movement as electrical current. This is the process by which all photovoltaic solar cells operate. Mastery of this process has had a profound impact on global energy generation. The Cu(InGa)Se₂ or CIGS thin-film solar cell, through advances in device characterization, processing, and materials, has achieved photovoltaic conversion efficiency of over 22% [1].

1.2 The Solar Boom

In the wake of substantial evidence supporting climate change [2], solar power has gained considerable momentum, not only because of its standing as an environmentally friendly technology, but also because of financial viability, and consumer accessibility. A multi-billion dollar industry has come to life around solar-energy technology in recent years. Manufacturing costs are continually decreasing while conversion efficiency continues to improve. Grid parity, the goal of the solar industry for decades, has been achieved in several areas and even eclipsed with reported costs as low as \$0.05/kWh [3] [4]. The state of California recently announced that it now obtains 10% of its total energy from solar, up from 0.9% 3 years ago. The U.S. installed 7.3 GW of solar generating capacity in 2015 to reach 27.4 GW of total installed capacity, enough to power 5.4 million homes. The amount of capacity installed in 2015 is projected to double in 2016 [5]

1.3 A Case for Thin-film photovoltaics

There are several types of solar energy conversion technologies. Solar-concentrators for thermal generation have been around for decades, but are seeing a decline in growth, mostly due to the relative success of low risk, utility-scale photovoltaics. Silicon wafer photovoltaics is an established technology that has dominated the solar panel market for several years. Silicon, other than being an abundant, and accessible material, has the advantage of a strong base of R&D due to the microelectronics and computing industry. It is a well understood material therefore high efficiency panels can be made fairly cheap. However, silicon-wafer technology has several fundamental drawbacks that may prevent it from continued dominance of the solar industry. The drawback that may prove to have the biggest impact is the energy and time cost of producing silicon wafers. Silicon itself is a poor absorber of sunlight due to its indirect bandgap, therefore wafers must be fairly thick. In order to collect generated carriers the wafers must be extremely pure to collect generated electrons. Making "solar-grade" silicon requires a large amount of energy and several steps that range from refining the raw silicon, to making monocrystalline ingots, to machining and assembly.

Thin-film solar cells (TFSC) are an alternative that can be made only a few microns thick, which promotes good electron collection and a small amount of material. TFSC's are designed to be excellent absorbers with direct band-gaps optimized to the solar spectrum. They perform well in varying temperatures and can be deposited on a variety of surfaces, making their applications numerous and versatile. The lower amount of materials reduces manufacturing costs and modern deposition methods result in a reduced manufacturing time. CdTe, amorphous silicon (a-Si), and CIGS are the current leading thin-film technologies [6]. CIGS solar-cells have long produced the highest efficiency TFSCs. Only in the last three years has CdTe begun to produce cells with comparable efficiency.

Chapter 2

CIGS SOLAR CELL TECHNOLOGY

2.1 CIGS

It is customary for a solar cell to be named after its absorber material. CIGS is shorthand for Cu(InGa)Se_2 , which has the chalcopyrite lattice structure, a direct bandgap, and for the cells in this study, is polycrystalline in nature. The grain boundaries of this material are relatively benign, which is important in mitigating recombination losses. A low density of electronically active defects at the grain surfaces due to sodium passivation of copper site defects is the common explanation [7].

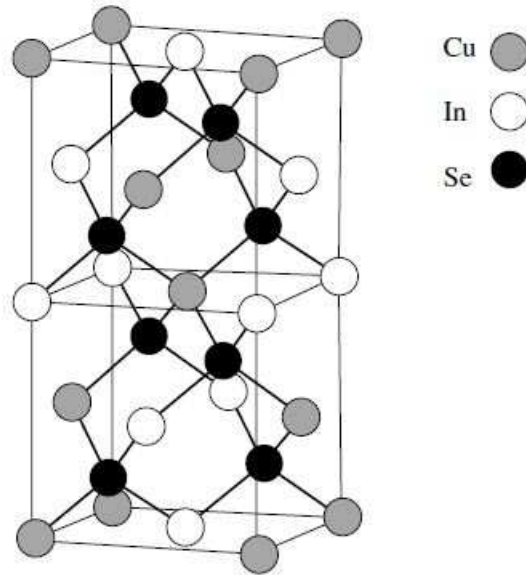


Figure 2.1: Unit cell of the chalcopyrite lattice [6]

CuInSe_2 has a bandgap (E_g) of 1.035 eV at low temperature, closer to 1.0 eV at room temp. This can be modified by the addition of Ga at In lattice sites, usually through co-deposition with CuGaSe_2 ($E_g=1.68$). High-efficiency cells typically have $\text{Ga}/(\text{In}+\text{Ga})$ ratios

between 0.2 and 0.3, and sometimes contain sulfur, which gives room for a range of E_g :

$$E_g(\text{eV}) = 1.0 + 0.13x^2 + 0.08x^2y + 0.13xy + 0.55x + 0.54y \quad (2.1)$$

where $x = \text{Ga}/(\text{In} + \text{Ga})$ and $y = \text{S}/(\text{S} + \text{Se})$ and is determined by a fit to experimental data [8].

2.2 Device Physics

When the p-type buffer layer and n-type CIGS absorber layer come into contact, a p-n junction is formed. The process is outlined in fig 2.2. The p-type material, although electrically neutral is doped to have an excess of holes (acceptor states). The n-type material, also electrically neutral, is doped to have an excess of electrons (donor states). When the two materials make contact, a junction forms.

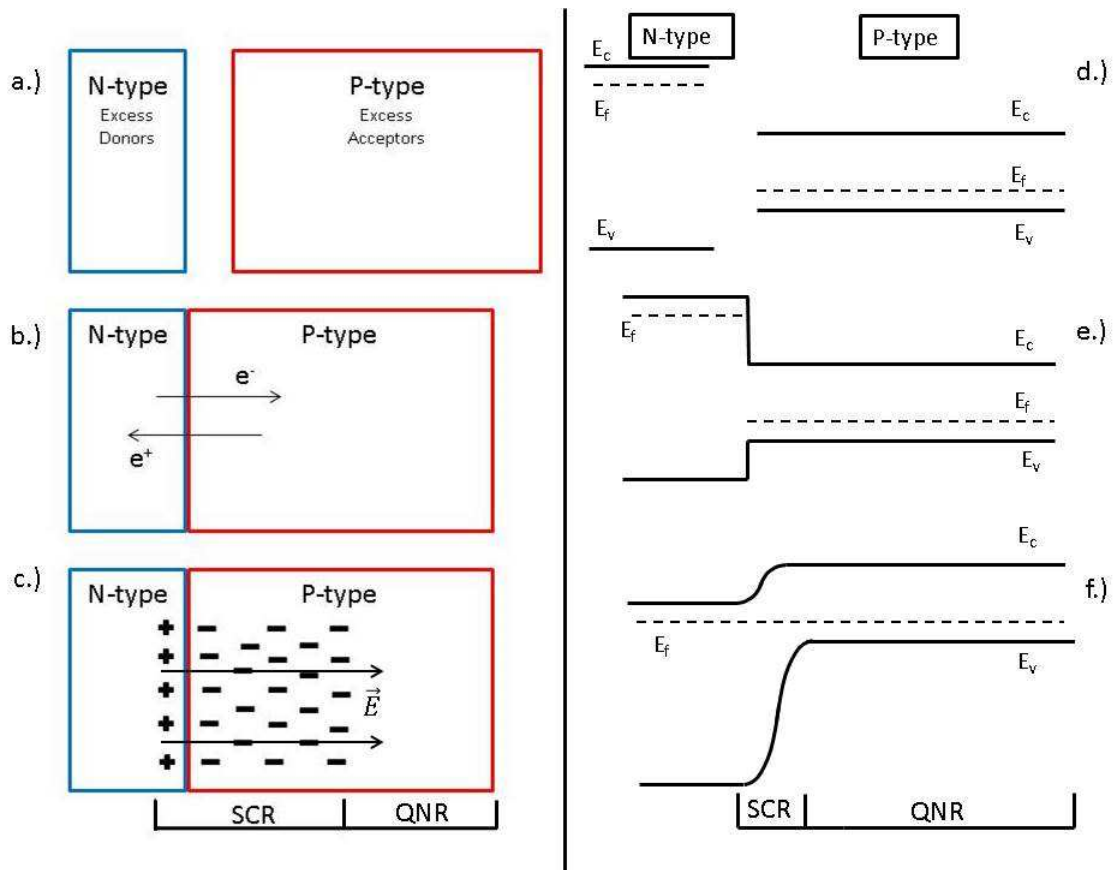


Figure 2.2: a-c : p-n junction and formation of the space-charge region, d-f: corresponding band diagrams

Since there is a concentration gradient of charge carriers between the two materials, electrons from the n-type material migrate to the p-type material and combine with holes, leaving behind a positively charged ion. Holes from the p-type material migrate to the n-type material to combine with electrons, leaving behind negatively charged ions (Fig 2.2b). This is known as diffusion current. The accumulation of charged ions in each material creates an electric field which is referred to as the "built-in field". The region the built-in field extends over is called the space-charge region (SCR). The SCR is stabilized when the drift current caused by the built-in field equals the diffusion current.

The width of the SCR in the p-type material W_p and in the n-type material W_n is based on the depletion approximation, which assumes the depleted charge has a box profile and is dependent on the doping densities, N_A for acceptor impurities, and N_D for donor impurities [9].

$$N_A W_p = N_D W_n \quad (2.2)$$

The band diagram shown in fig 2.2f is a useful way of looking at a p-n junction. A charge carrier can either be bound to an atom (in the valence band) or able to move freely throughout the material (in the conduction band). The Fermi-Dirac distribution describes the occupancy of states in a material, and the Fermi level is the energy of average occupancy, essentially the average electron energy. In an n-type semiconductor, (which has a larger concentration of free electrons) the Fermi level lies closer to the conduction band, while in a p-type semiconductor (low concentration of free electrons) the Fermi level lies closer to the valence band fig 2.2d. To satisfy the zero current condition associated with thermal equilibrium, the Fermi level throughout the sample must be constant. When put in contact, the Fermi levels of the two materials line-up, causing a shift in band alignment fig 2.2e-f. The SCR can be looked at as a shift in the energy bands at the junction. Electron hole pairs generated in the SCR are swept across the band and collected at the electrical contacts. This is called drift current. The part of the absorber that is not part of the built-in field is called the quasi neutral region (QNR). Electron-hole pairs generated in this region are not immediately swept across the junction. Their movement is dependent on carrier lifetime and diffusion length, also their

direction of movement is random. Due to the absorption capability of CIGS the width of a cell may need to be large enough to allow for a depletion region capable of collecting deeper penetrating long wavelength photons and to avoid recombination losses that may result from generation near the back contact junction. An example CIGS band diagram is displayed in fig 2.3.

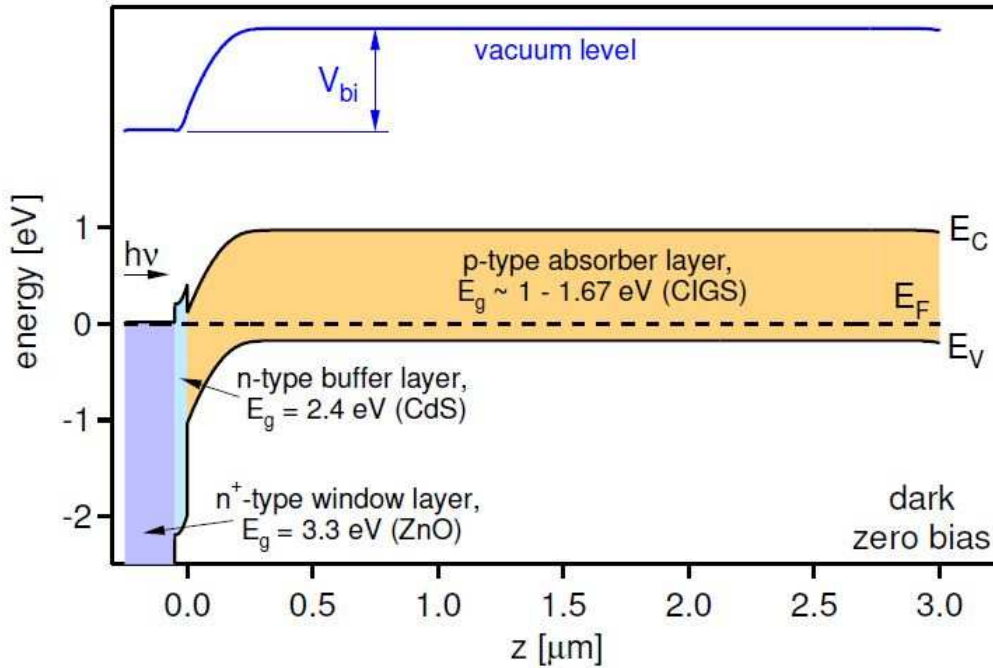


Figure 2.3: CIGS band diagram[10]

2.3 Device Structure

The basic CIGS thin-film cell structure can be seen in figure 2.4. CIGS cells generally have a substrate configuration, which refers to the orientation of the cell while in operation. The substrate material is the base or bottom of the cell. Film layers are deposited on the substrate, and light is incident on the top side of the structure.

There are multiple options for the substrate material. Soda-lime glass is cost effective, and the diffusion of sodium through the back contact material into the absorber provides additional benefits, such as passivation of acceptor like defects, and suppressing the formation

of ordered defect compounds (Wei). Aside from this, the coefficient of thermal expansion of soda-lime glass is similar to that of CIGS, and so the cooling from crystal growth temperatures causes negligible stress to either material. Flexible metallic foil is lightweight and malleable which works with the flexible nature of CIGS cells. Additionally there are novel plastic substrates used by several manufacturers that increase the versatility of CIGS technology.

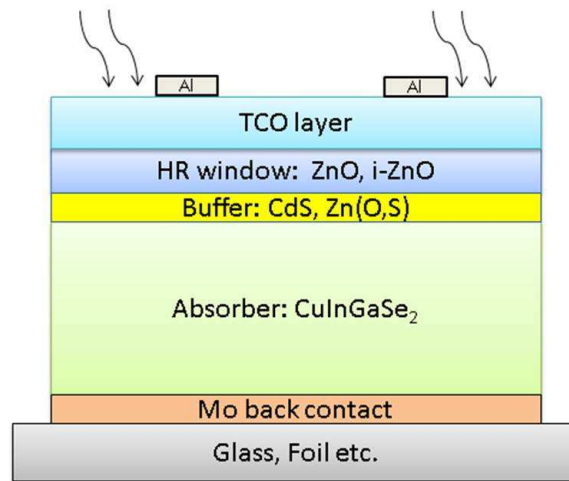


Figure 2.4: CIGS cell structure

The back electrical contact deposited directly on the substrate is generally sputtered molybdenum, with a thickness dependent on sheet-resistance requirements. During deposition of CIGS an interfacial layer of MoSe_2 forms, which does not degrade device performance and may promote formation of an ohmic contact. Several methods are used to deposit 1-3 μm of p-type $\text{Cu}(\text{InGa})\text{Se}_2$ which will be discussed in section 2.5. A p-n heterojunction is formed by adding an n-type layer of CdS or $\text{Zn}(\text{O,S})$, by chemical bath deposition or sputtering. While CdS is good for forming a junction with CIGS, it has a band gap of 2.5 eV ($\lambda \approx 500 \text{ nm}$), which results in significant absorption of the blue photons in the solar spectrum, and provides a non-trivial conduction band offset that impedes photocurrent flow. CdS is deposited in a very thin layer to limit the absorption losses. A high resistance (HR), highly transmissive, ZnO window layer is commonly deposited on top of the CdS layer.

The benefits of which could come from filling in pinholes in the thin CdS, which could form ZnO/CIGS diodes in parallel with the CdS/CIGS junction, and adding a layer of protection from the sputtering process. Lastly a transparent conducting oxide (TCO) layer of doped ZnO or In₂O₃:Sn (ITO) is deposited to facilitate lateral current collection. Cells are typically finished with aluminum gridlines that can be defined with photolithography or evaporation with an aperture mask [6].

2.4 CIGS Variations

Six labs including the National Renewable Energy Laboratory (NREL) labeled A, the Institute for Energy Conversion (IEC) labeled B, and four companies (labeled C-F) each contributed multiple cells to this project. All cells submitted are approximately 1 cm² or smaller and have high efficiency, in the range of 14% to 20%. Each lab builds a high efficiency cell very differently. Table 2.1 gives a summary of the substrate used by each lab, their absorber deposition process, absorber material, buffer material, and cell structure. The highest efficiency cell from each lab was measured and used for comparison.

Table 2.1: Participant processing details

Lab	Substrate	Absorber Process	Absorber	Buffer	Cell Structure
A	Glass	Co-evap. (3-Stage)	Cu(InGa)Se ₂	CdS	ZnO:Al/i-ZnO/CdS/CIGS/Mo
B	Glass	Co-evap. (3-Stage)	(AgCu)(InGa)Se ₂	CdS	ITO/i-ZnO/CdS/ACIGS/Mo
C	Steel (R2R)	Co-Sputtering	Cu(InGa)Se ₂	CdS	ZnO:Al/i-ZnO/CdS/CIGS/Mo
D	Steel (R2R)	Co-evap. (3-Stage)	Cu(InGa)Se ₂	CdS	ITO/i-ZnO/CdS/CIGS/Mo
E	Glass	Precursor Reaction	Cu(InGa)(SSe) ₂	CdS	ZnO:B/ZnO/CdS/CIGSSe/Mo
F	Glass	Precursor Reaction	Cu(InGa)(SSe) ₂	Zn(O,S)	ZnO:B/ZnO/Zn(O,S)/CIGSSe/Mo

Three-stage co-evaporation is a technique that involves evaporation of the different materials in three stages, often resulting in a graded bandgap. In, Ga and Se are first evaporated in the chamber, then Cu with Se. The materials interdiffuse on the surface into CIGS. This results in a copper rich composition. In, Ga, and Se are evaporated again in the third stage

to result in a Cu deficient layer. A Cu deficient junction and a Cu rich bulk region have been empirically found to make the most efficient cells [11]. Co-sputtering involves bombarding multiple targets with an ion beam to kick off particles in an argon or selenium rich atmosphere. Such ejected particles are not in their thermodynamic equilibrium state and so deposit on a substrate placed in the chamber. Precursor reaction involves deposition of a precursor film containing Cu, In and Ga, which is then reacted at high temperatures with H_2Se and sometimes S to form $\text{Cu}(\text{InGa})\text{Se}_2$. There is ample room for variation of elemental deposition in each technique by varying the elemental flux with co-evaporation, or sputter yield.

- Lab A is the closest to the "standard" CIGS cell of the group in that it does not use novel materials to improve performance.
- Lab B uses silver deposited in the absorber to help increase the bandgap, and an ITO conducting layer.
- Lab C in addition to using a flexible stainless steel substrate, deposits a $\text{Cu}(\text{InGa})\text{Se}_2$ through co-sputtering and uses a (ZnO:Al) layer.
- Lab D also uses roll to roll deposition onto a flexible stainless steel substrate, but with co-evaporation, similar to cells A and B.
- Labs E and F deposit on glass through a precursor reaction. Lab F is cadmium free, using Zn(O,S) instead of CdS. Both use a proprietary TCO layer, and both have added sulfur in their absorber layer.

Some of the cells are more similar than others, and we will use these similarities to learn about the impact of their differences. E and F will often be compared side-by-side because of their similar deposition processes and similar TCO layers. Labs E and F are also the only labs that use sulfur in their absorber layer. Labs A and B will be compared frequently to look at the effect of Ag in the absorber layer. A and D will serve as a good comparison because of their similar deposition processes on different substrates. Table 2.1 shows differences in

processing and materials while the following chapters will reveal more intricate details of processing and varying performances. Chapter 3 will deal with measurement techniques used at Colorado State University. Results and comparison of measurements are found in chapter 4 with interpretation and conclusions in chapter 5.

Chapter 3

SOLAR CELL CHARACTERIZATION

This chapter will discuss electrical and spatial measurement techniques employed in this study. Emphasis will be on the physical mechanisms behind each technique, the attainable information, and the experimental set-ups.

3.1 Current-Density vs. Voltage

The most significant parameter associated with a solar-cell is conversion efficiency.

$$\eta = \frac{P_{MP}}{100 \text{ mW/cm}^2} \quad (3.1)$$

Where P_{MP} is the maximum output power density of the cell and 100 mW/cm^2 is the approximate incident illumination power density under air mass 1.5 (AM 1.5) illumination conditions. AM 1.5 illumination is representative of the sun's illumination conditions on the earth's surface. It takes into account atmospheric effects on the sun's spectra as well as angle of incidence. Another important parameter, fill factor is,

$$FF = \frac{P_{MP}}{J_{SC}[\text{mA/cm}^2] \cdot V_{OC}[\text{V}]} \quad (3.2)$$

where P_{MP} is $J_{MP} \cdot V_{MP}$. J_{SC} is the short-circuit current density and V_{OC} is the open circuit voltage. Parameters J_{SC} , V_{OC} , FF , and η are taken from current-density vs. voltage (JV) measurements, in which current is measured over a changing voltage bias and normalized to the cell area. Fig 3.1 shows a typical set of JV curves in the dark and at standard illumination.

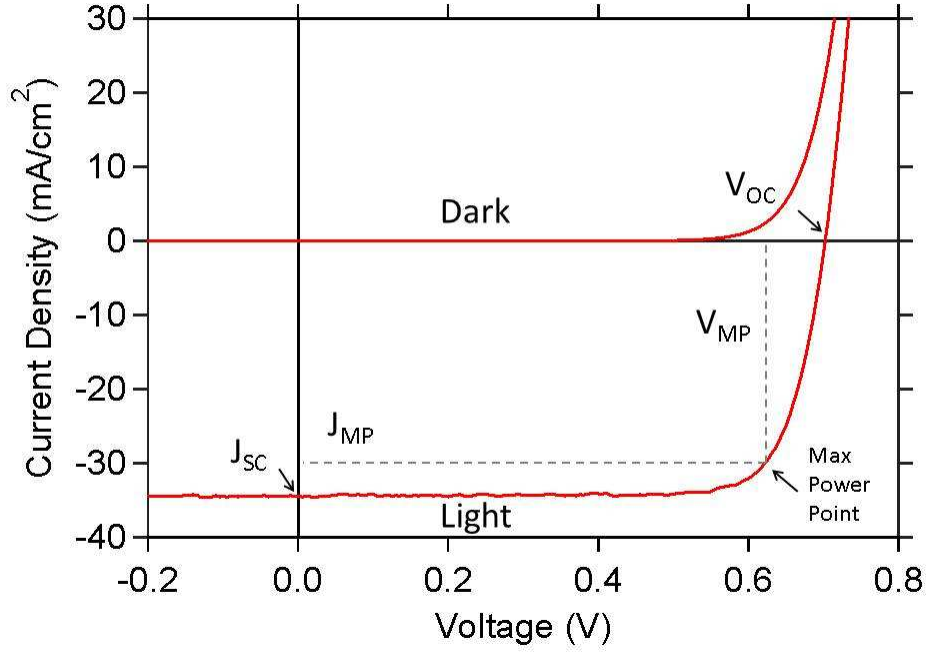


Figure 3.1: Representative JV curve

In the dark there is no change in current until the voltage is sufficiently high enough to overcome the built in field at which point current becomes exponentially large. The J-V curve drops into the fourth quadrant when illuminated as J_L (light generated current) becomes dominant.

An important and relevant way of looking at a solar cell in terms of electrical characterization, is to model the cell as a circuit. Fig 3.2 is the equivalent circuit of a solar cell. All of the displayed parameters are measurable and have a real effect on cell operation. The operation of this circuit is described by the diode equation:

$$J = J_0 \left[e^{\frac{q(V-JR_S)}{nkT}} - 1 \right] + \frac{V - JR_S}{r_{SH}} - J_L \quad (3.3)$$

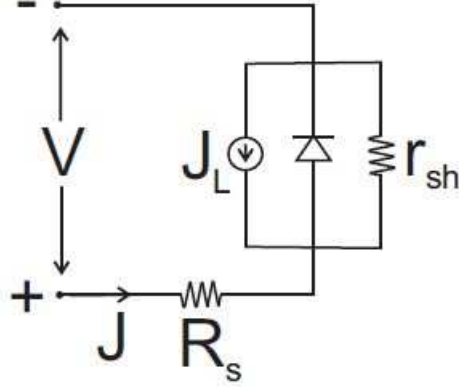


Figure 3.2: Equivalent circuit diagram, from[8]

J_L can be described as:

$$J_L(V) = J_{L0} \cdot \eta_C(V) \quad (3.4)$$

with J_{L0} being the optically limited light generated current and η_C a voltage dependent collection function. J_0 is the saturation current density given by:

$$J_0 = J_{00} \cdot \exp \left[-\frac{\phi_b}{nkT} \right] \quad (3.5)$$

The prefactor J_{00} is dependent on the specific recombination mechanism that dominates the forward current J_0 . n , is the diode quality factor which ranges between 1 and 2 and is dependent on energies of defects that act as dominant trap states. ϕ_b is the barrier height which is the energy difference between the fermi level and the conduction band. In most cases doping density of the absorber is large enough that it can be considered to be equal to the bandgap. T is temperature, k is the the Stefan-Boltzman constant, q the elementary charge, R_s and r_{sh} are representations of the losses that occur in series or in parallel with the primary diode respectively [12].

The J-V measurement system used in this project used a Keithley 2401 sourcemeter for applied bias, current and voltage measurements. A xenon arc-lamp with filters is used as a solar simulator. The system is calibrated to AM 1.5 conditions using a Si reference cell.

3.2 Quantum Efficiency

Quantum efficiency (QE) is a measure of the number of collected electrons to the number of incident photons. QE measurements are commonly used to determine the losses responsible for reducing the measured J_{sc} from the maximum achievable photocurrent fig 3.3. When measured at 0V bias, the integral of $QE(\lambda)$ can be used to calculate J_{sc} :

$$J_{sc} = q \cdot \int_0^{\lambda=\infty} QE(\lambda) \cdot AM\ 1.5(\lambda) d\lambda \quad (3.6)$$

where q is the elementary charge and AM 1.5 (measured in photon-flux units) is the solar spectrum standard used in photovoltaic measurements.

Measured QE, or external QE (EQE), is that of a finished cell which does not account for losses due to reflection. IQE or internal QE accounts for reflection losses and is defined as $QE/(1-R)$ (where R represents total reflection losses) and is a measure of the QE of the absorber material rather than the entire cell. Other J_{sc} losses can be accounted for through an analysis of QE measurements illustrated by fig 3.3.

QE measurements also provide an estimate of the CIGS bandgap, E_g , which can be found by using the maximum absolute value of the derivative of QE with respect to wavelength.

$$E_g = \max \left| \frac{d(QE)}{d\lambda} \right| \quad (3.7)$$

This process corresponds to a sharp energy cutoff, which for graded band-gap absorbers would be an average.

QE was measured using light from a halogen bulb, which passes through an Acton Spectra Pro 150 monochromator. The monochromatic light is chopped by an SRS SR450 chopper and focused on an area of the cell. The cell current output is amplified by a SRS SR570 preamplifier. The signal is measured by a SR870 lock-in amplifier, which is locked to the chopper frequency. A 620 nm long-pass filter is inserted into the beam after the sweep passes 650 nm to remove second order monochromator peaks [13]. Reflection measurements were made on a Perkin-Elmer Lambda 2 Spectrometer.

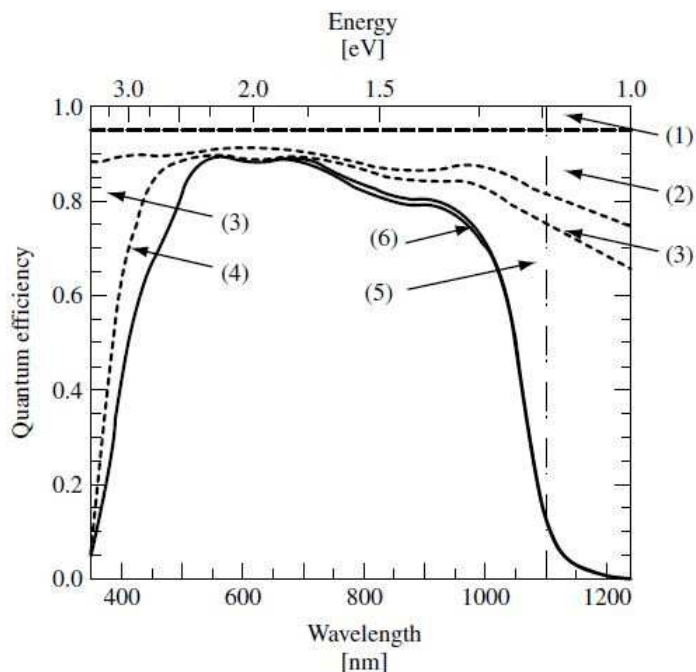


Figure 3.3: QE curve from a CIGS cell w/ J_{SC} losses labeled [1]

Above is a representative QE curve of a CIGS cell. The individual losses corresponding to figure 3.3 are:

1. Shading from the front contacts
2. Front surface reflection
3. Absorption in the ZnO layer where $E_g = 3.3$ eV
4. Absorption in the CdS layer where $E_g = 2.4$ eV. The loss below E_{gap} of CdS is proportional CdS thickness, since it is commonly observed that carriers generated in CdS are not collected
5. Incomplete CIGS absorption near the band gap. Band-gap gradients affect the steepness of the curve in the long wavelength region
6. Incomplete CIGS collection which has been shown to be affected by absorber thickness.

[6]

3.3 Capacitance Measurements

Capacitance-frequency (C-F) and capacitance-voltage (C-V) measurements work on the principle that a p-n junction can be modeled as a parallel plate capacitor, with a capacitance (C) of:

$$C(V) = \frac{\epsilon\epsilon_0 A}{W(V)} \quad (3.8)$$

A is cell area, W is width of the depletion region, and ϵ and ϵ_0 are the permittivity of the semiconductor material and permittivity of free space respectively. W for a one sided abrupt junction:

$$W(V) = \sqrt{\frac{2\epsilon\epsilon_0(V_{bi} - V)}{qN_p}} \quad (3.9)$$

where q is the elementary charge, V_{bi} is the built in potential, V is the applied voltage and in CIGS cells N_p is the doping concentration of the absorber layer. These types of measurements are not definitive because of the typically large density of trap states found in thin-film solar-cells which cause the boundary of the depletion region to be imprecise. However, the measurements do provide approximate information. Capacitance as a function of frequency is first measured at several voltage biases, to check for possible dispersion. A flat area on the C-F curve where C does not vary is chosen as a stable AC frequency for use in C-V measurements, around 50 kHz in fig 3.4.

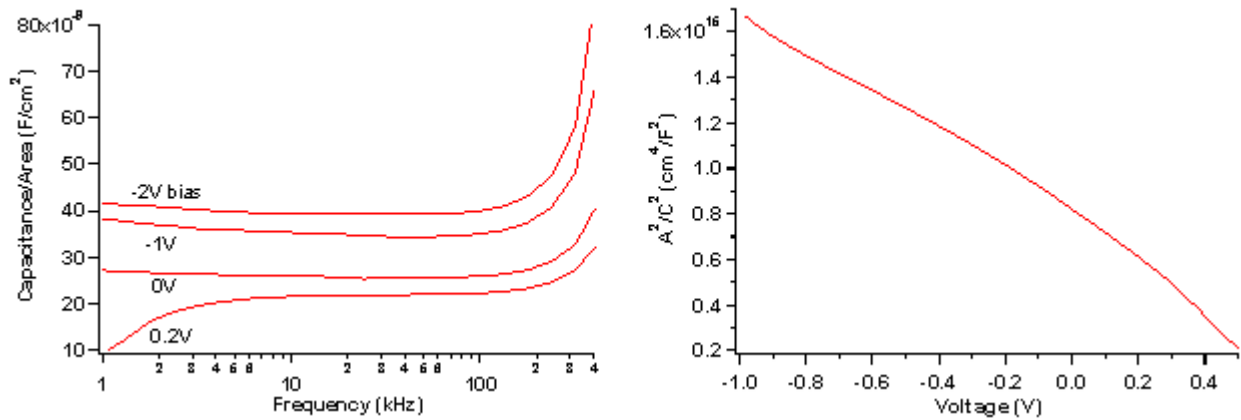


Figure 3.4: left: Capacitance-frequency, right: A^2 / C^2 vs voltage of a CIGS cell

The sudden rise in the curve close to 1000 kHz is an artifact of LC resonance due to the inductance of the cable used. Combining eqns 3.8 and

$$\frac{A^2}{C^2} = \frac{2(V_{bi} - V)}{q\epsilon\epsilon_0 N_p} \quad (3.10)$$

The intercept of a plot of A^2/C^2 vs. V , fig 3.4 (right), gives V_{bi} , and the slope yields doping concentration N . Since in the depletion approximation the capacitance originates solely from the edge of the depletion region, rearrangement of eqn 3.10 to solve for N_p and taking the derivative of $d(C^{-2})/dV$ and substituting in eqn 3.8:

$$N_p = \frac{C^2}{qWA} \cdot \frac{\Delta V}{\Delta C(V)} \quad (3.11)$$

We can obtain the doping concentration as a function of distance from the junction [14] [9]. A representative plot is shown in fig 3.5.

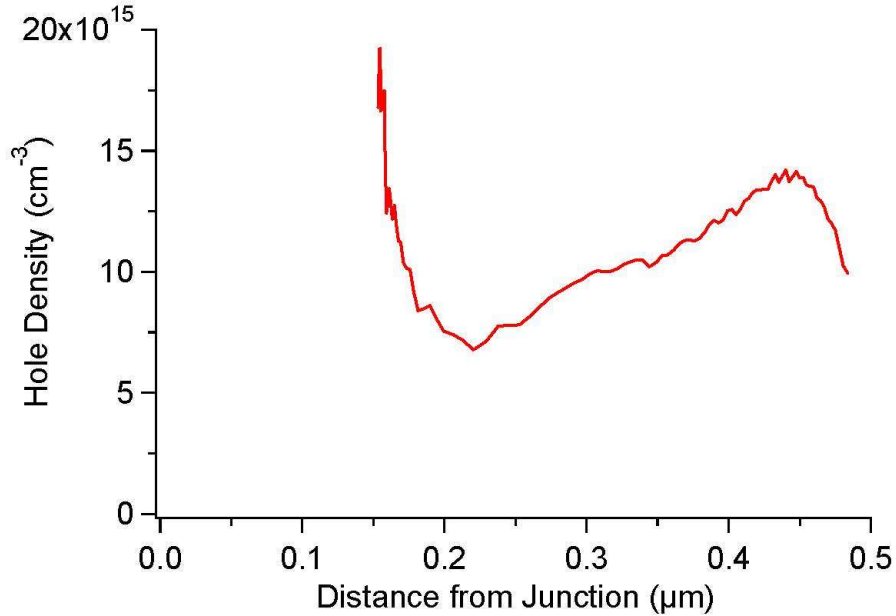


Figure 3.5: Hole density vs distance from junction

For capacitance measurements a HP 34401A multimeter, HP 4192 A LF Impedance Analyzer and Keithley 230 power supply were used.

3.4 Electroluminescence

The first spatial characterization method to be discussed is electroluminescence (EL). EL is the spontaneous emission of radiation in a semiconductor as a result of injection of free carriers. An injection current is applied to the cell and the electrons in the conduction band recombine with holes in the valence band. Most carriers recombine non-radiatively, but some fraction cause the emission of photons, that fraction being dependent on the material. Put simply EL measurements treat a solar cell as an LED. A constant current is applied to the cell and radiated photons are detected by a CCD camera. A CCD is a detector of photon intensity rather than a spectral detector. This intensity is converted to a pixel value and an image is assembled. Images in this study are divided by time of exposure and represent an emission rate relating to the quality of a cell's absorber. Analysis of EL images can identify locations of weak activity, defects and inhomogeneities. One advantage of EL is that measurements can be performed in a relatively small amount of time, quickly identifying processing faults [15].

3.5 Light-Beam-Induced Current

Light beam induced current (LBIC) provides topographical performance data of the cell. Specific details or defects can be analyzed and small areas can be isolated. For the measurements taken in this study a 638 nm diode laser was rastered across the total cell area and the cell current was measured. LBIC works complementary to EL in that defects identified in EL can be looked at in depth with LBIC. LBIC measurements use an SRS SR540 mechanical chopper, a Chroma 12061 multimeter, a Thor Labs LDC 201C VLN laser diode controller, a SR570 Preamplifier, and an SR 810 Lock-In.

3.6 Scanning Electron Microscopy and Auger Profiling

Collaborating laboratories performed scanning electron microscopy (SEM) and Auger emission spectroscopy (AES) measurements on representative cells from each lab in this project. SEM imaging is divided into that making use of secondary electrons and backscattered electrons, resulting in different contrasts in the images and thus providing information on compositions, microstructures, and surface potentials. In this study SEM was used to obtain an image of the cross-section of a cell. With this image we can get information about a cell's topography and composition.

AES measurements performed on a Physical Electronics 670 field-emission scanning Auger spectrometer at NREL provide valuable insight into the makeup of each cells absorber material. The Auger profiles allow understanding of possible effects taking place at buffer/absorber and absorber/back-contact junctions as well as the band-gap and any gradients. AES utilizes the Auger effect whereby an energetic electron moves to a lower energy state and gives its energy to another electron which is ejected from the material. Lower energy-state vacancies in many instrument configurations are created by bombardment by an electron beam. The ejected electrons are collected and their energies give an indication of the elemental composition of the material. Auger is performed while sputtering through the depth of the material and provides info on the elemental composition through the depth of the cell [14]. Sputter rate was calibrated on a 100 Å Si wafer calibrated at 151 Å/min, however sputter rates depend on the material and may require a correction.

Chapter 4

MEASUREMENTS AND ANALYSIS

This chapter will look at measurement results with an emphasis on comparison between cells, and identification of the features and mechanisms contributing to the identified parameters.

4.1 J-V

Table 4.1 contains some cell parameters extracted from J-V measurements as discussed in section 3.1, and includes cell area. The parameters below were determined from J-V data using the current-voltage analysis program (CurVA), developed by M.Gloeckler. CurVA uses several different methods of plotting the diode equation for a solar cell (eqn 3.3), coherent with the methods for extracting cell parameters found in [12].

Table 4.1: J-V performance parameters

Lab	Area[cm ²]	V _{OC} [mV]	J _{SC} [$\frac{\text{mA}}{\text{cm}^2}$]	FF[%]	η [%]	J ₀ [$\frac{\text{mA}}{\text{cm}^2}$]	r _{sh} [$\Omega \cdot \text{cm}^2$]	R _s [$\Omega \cdot \text{cm}^2$]	n
A	0.42	701	34.3	80.7	19.4	2.5e-8	1.1e4	0.3	1.3
B	0.4	742	33.0	77.8	19.1	2.9e-7	5.5e3	0.4	1.6
C	0.42	698	32.3	77.4	17.5	1.3e-6	6.3e3	0.2	1.6
D	1.0	659	35.5	68.6	16.0	1.8e-5	2.3e2	0.6	1.8
E	0.42	571	34.6	72.3	14.3	1.1e-5	2.3e3	0.8	1.5
F	0.53	669	38.3	73.2	18.8	7.5e-6	1.1e3	0.4	1.7

The current record efficiency CIGS cell is held by Solar Frontier at 22.3% [1]. While all the cells involved in the study have relatively high efficiencies, no single manufacturer is dominating in every category. (B) has the highest V_{OC} which is typically coincident with having a large band-gap, (F) has the highest J_{SC}, typically coincident with having

a low band-gap. (A) has the highest FF, lowest diode quality factor n , lowest value of recombination current, J_0 (eq 3.5) and highest efficiency η . Cell D performed lowest in nearly every category. JV curves under standard illumination are shown in fig 4.1. The JV curves for all cells are well-behaved. Neither r_{sh} or R_s (fig 3.2) have significant impact on the curves.

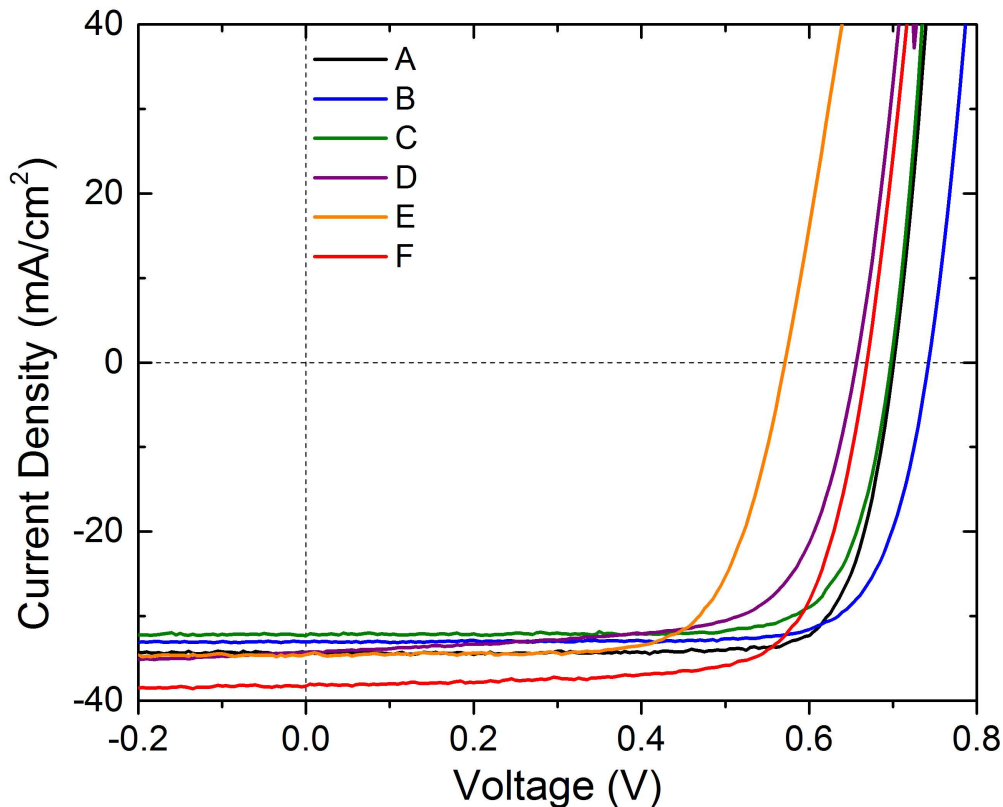


Figure 4.1: J-V under standard illumination

The Shockley-Queisser (S-Q) limit defines the theoretical maximum efficiency obtainable by a single junction diode with band-gap energy E_g , given a set of specific assumptions. To summarize, the assumptions are: (i) The probability of generating an electron-hole pair for photons with energy E_g is unity (ii) All photogenerated charge carriers thermalize to the band edges (iii) The collection probability for all photo-generated electron-hole pairs is unity.

(iv) The only loss mechanism is the spontaneous emission of photons by radiative recombination of electron-hole pairs as required to satisfy the principle of detailed balance. [11]

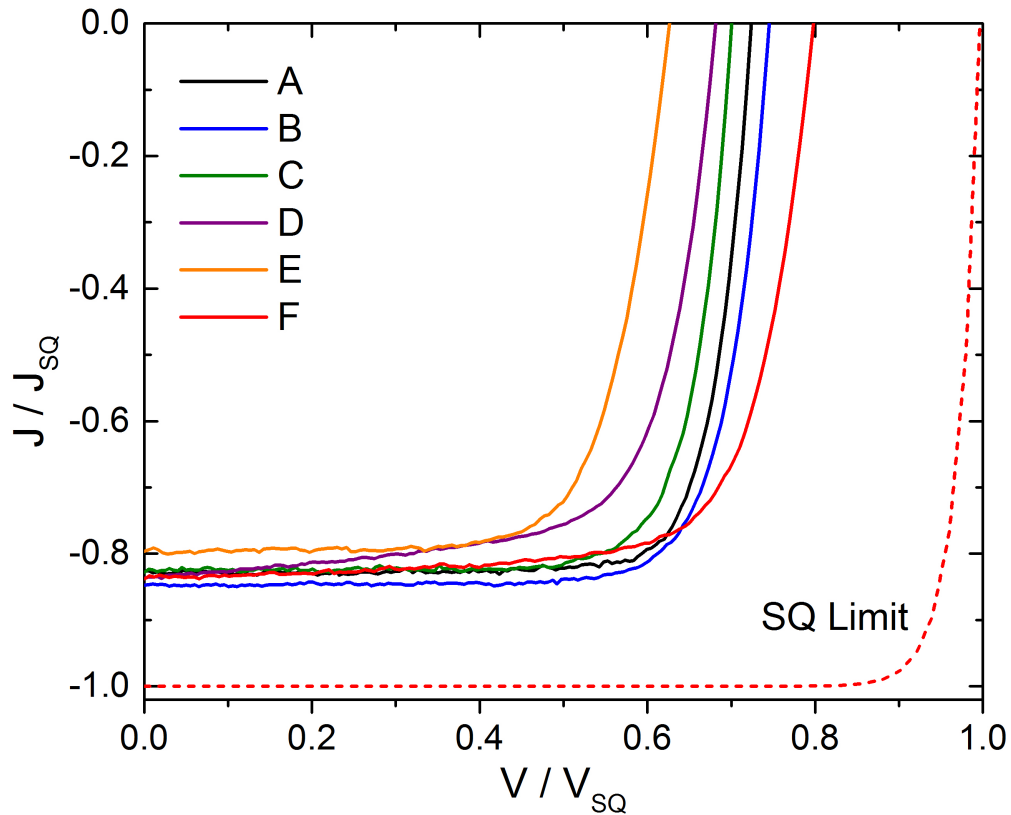


Figure 4.2: J-V normalized to S-Q limit

By normalizing to the S-Q limit we can see how well each cell is optimized. Stated a different way, where each cell lies with respect to its theoretical limit. The J-V curves in fig 4.2 are the curves from fig 4.1 that have been normalized to the S-Q limit. While each cell in this study has very good efficiency, there is still ample room for improvement in both J_{SC} and V_{OC} . J_{SC} values of all cells corresponded to collecting 80-85% of all photons above the band-gap. V_{OC} values ranged between 65-80% of maximum. After normalization cell F has the highest V_{OC} relative to the theoretical limit. Fill factors were quite good, all within 82-95% of the maximum.

4.2 QE and Reflection

Quantum efficiency and reflection of each cell were measured in parallel and the internal quantum efficiencies (IQE) are compared in fig 4.3. The IQE curves for all the cells are quite good, nearly 100% over a broad part of the solar spectrum.

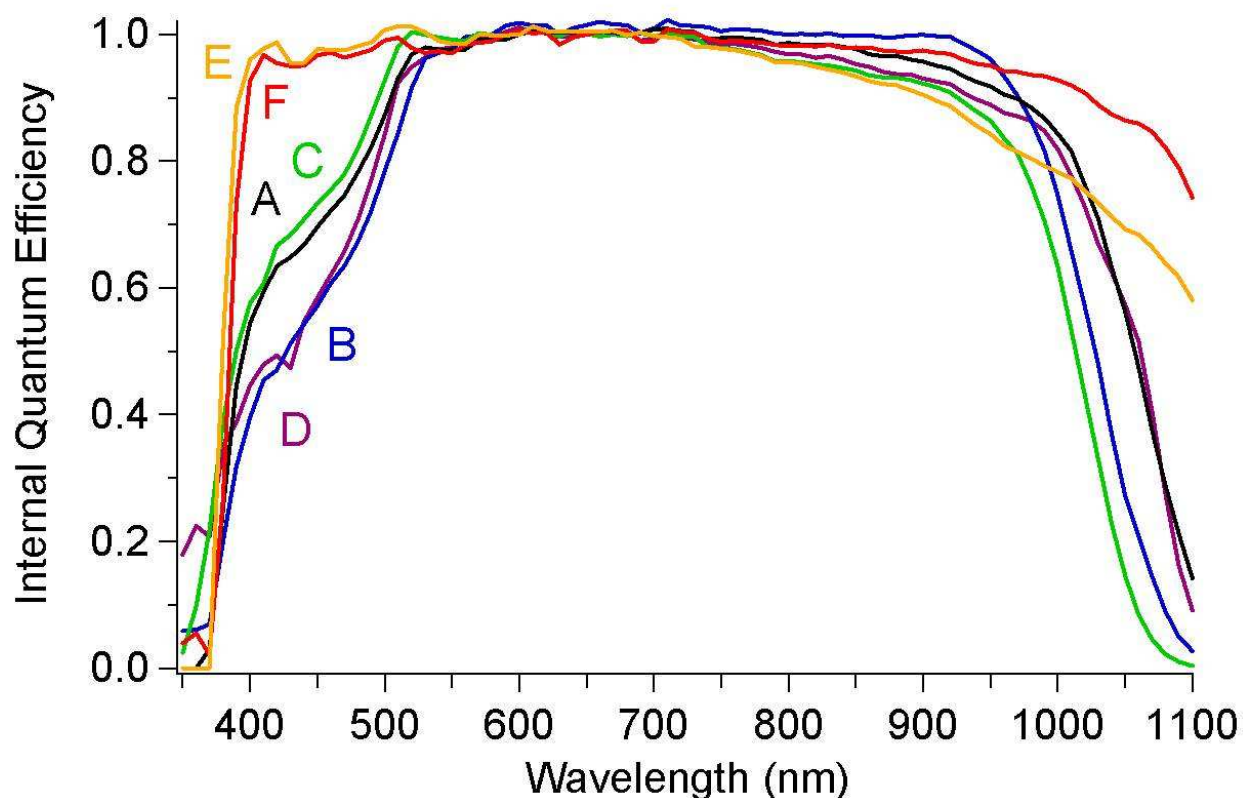


Figure 4.3: Internal quantum efficiency

The most striking thing about fig 4.3 is that labs E and F have much greater QE at shorter wavelengths. Cells B and D have the lowest performance in this area. Improved performance above the CdS bandgap ($\lambda < 500$ nm) likely has to do with buffer layer thickness. It is possible that the addition of sulfur to the absorber in cells E and F allows for a thinner CdS layer. It is also worth noting that the Zn(O:S) buffer layer found in cell F seems to perform about as well as the CdS in cell E. Lab B maintains the highest QE in the mid range staying at almost unity until about 950 nm. The well defined shoulder on the right side of cell B's

curve suggests good mitigation of deep penetration losses toward the back of the cell. The fall off at longer wavelengths in each curve reflects the differences in bandgap between cells, corresponding to eqn 3.7.

Lab F and Lab E both have gradual slopes in IQE that extend beyond measurement capabilities, which also coincides with lower values of E_g . Though our measurements only extend out to 1100 nm it is not an unreasonable extrapolation based on the slope of cells E and F to say their QE is non-zero out to 1200 nm. Both show signs of incomplete collection at longer wavelengths with cell F performing much better.

Table 4.2: J_{SC} losses [$\frac{mA}{cm^2}$]

Lab	E_g^{QE} [eV]	J_{sc}^{ideal}	J_{SC}^{QE}	Reflection	Window	Deep Penetration
A	1.17	39.7	35.5	1.2	1.7	1.3
B	1.22	37.6	33.6	1.5	2.1	0.5
C	1.22	37.7	33.2	1.6	1.3	1.6
D	1.18	39.3	34.1	1.5	2.0	1.5
E	1.09	43.0	36.8	3.2	0.1	3.0
F	1.05	45.3	41.4	1.8	0.3	1.8

Table 4.2 quantifies the values of J_{sc} losses by type of loss in accordance with fig 3.3. J_{sc}^{ideal} is the value of J_{sc} derived from bandgap:

$$J_{SC}^{ideal} = q \cdot \int_0^{\lambda_g} AM 1.5(\lambda) d\lambda \quad (4.1)$$

and

$$J_{SC}^{ideal} = J_{SC}^{QE} + \text{Reflection} + \text{Window} + \text{Deep Penetration} \quad (4.2)$$

Where λ_g is the equivalent E_g wavelength. Reflection, corresponds to losses from grid shading and reflection, and was measured from 400 nm to λ_g . Window corresponds to buffer layer, window layer and TCO absorption, and represents losses from 400 nm to 650 nm. Deep penetration corresponds to incomplete absorption losses from 650 nm to λ_g . Cell E in

particular stands out as having the highest reflection, deep penetration and total J_{sc} losses, but the lowest window losses, by a significant margin in each case.

4.3 Capacitance

C-V measurements were taken in general at 50 kHz AC voltage as determined from C-F data. From eq. 3.10 the slope of a plot of $(A/C)^2$ vs. V fig 4.4 reveals relative doping concentration. Cells C, E and F form fairly straight lines and thus seem to have somewhat uniform doping concentrations. Attempts were made to take each cell from a reverse bias voltage of -1V to a forward bias voltage of 1 V. Most cells could only be biased to ~ 0.6 V forward bias, however in the case of cell D, large negative or forward biases were beyond the cell's capability. Diode quality factor (n) for cell D was the highest measured in J-V. Since n is indicative of trap state concentration, poor performance as a capacitor is to be expected. Note that the plot of cell B is not included as it is a decade larger than the rest of the group, though its general shape is similar to cell C.

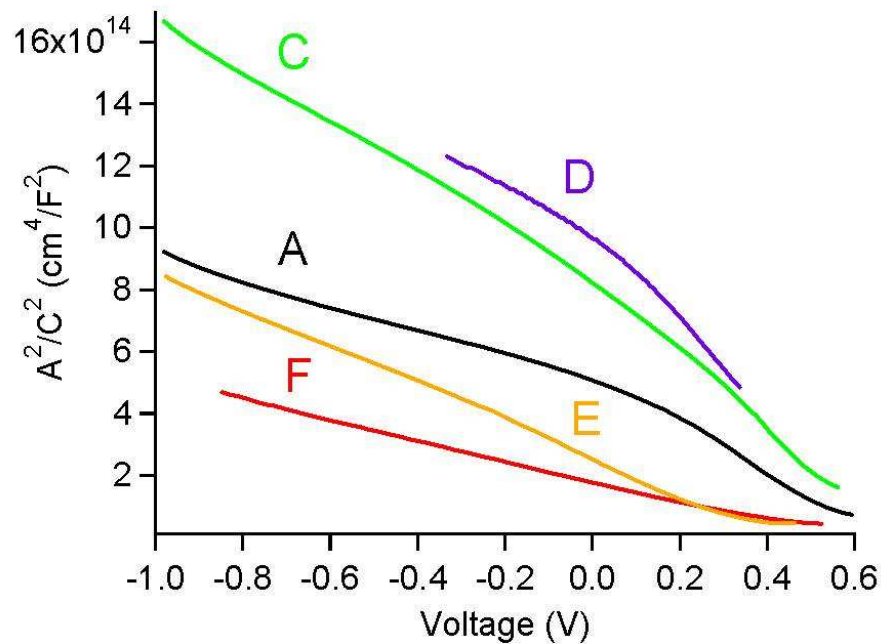


Figure 4.4: A^2 / C^2 vs Voltage

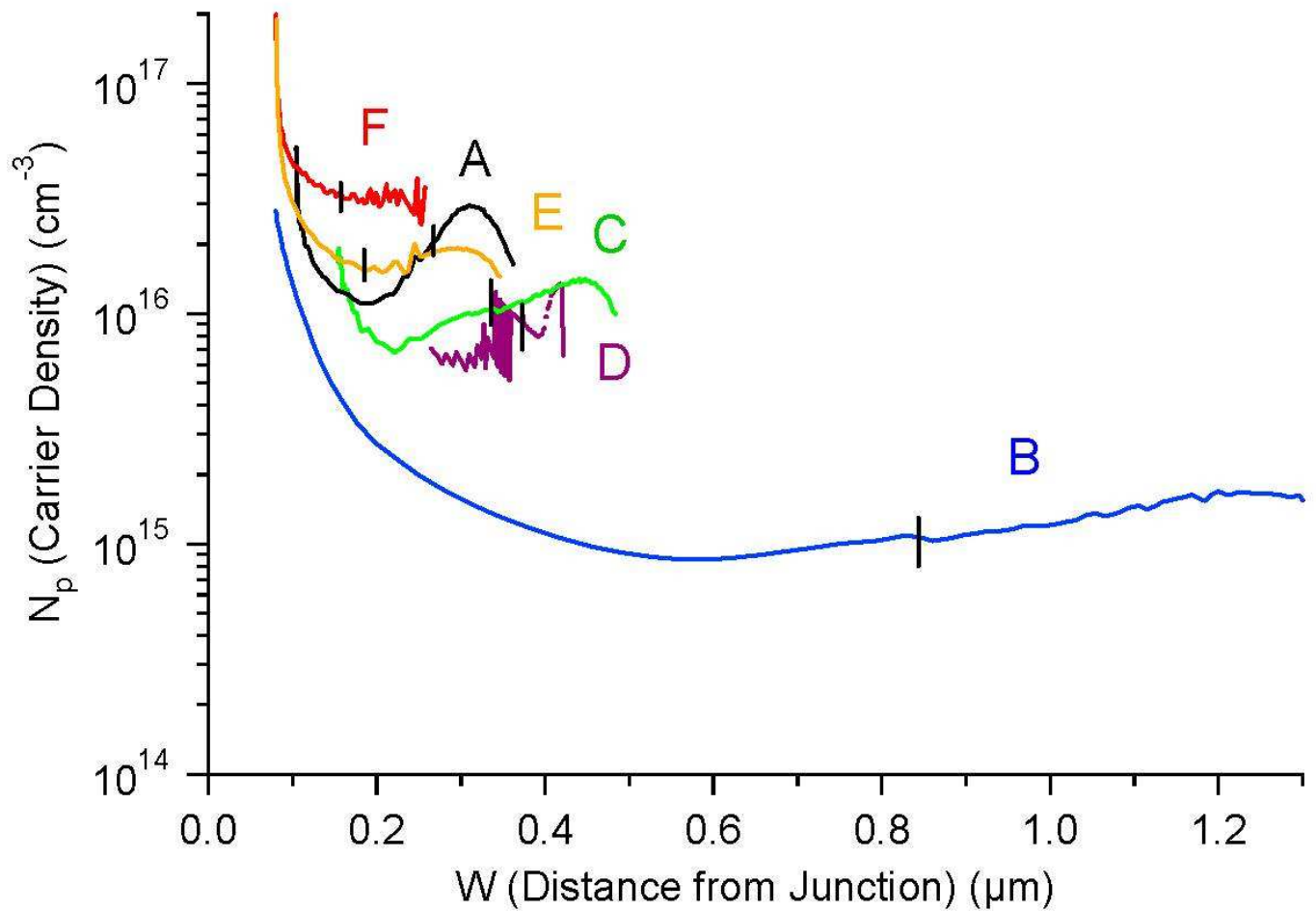
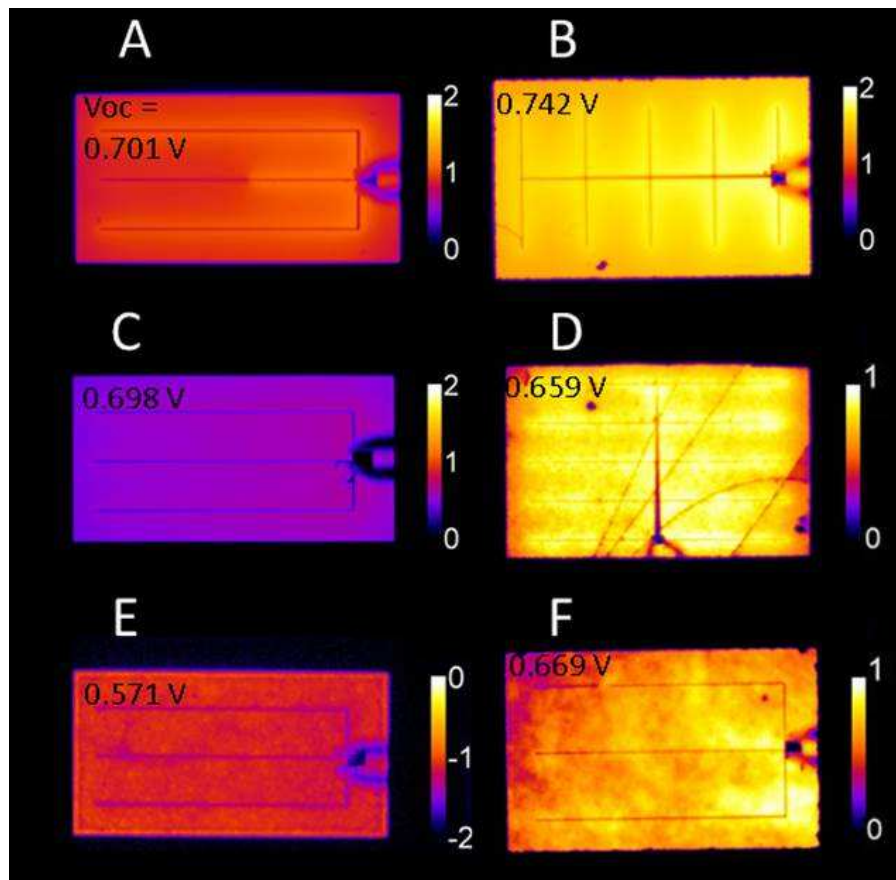


Figure 4.5: Hole Density vs Distance from Junction

Fig 4.5 shows N_p vs. W with locations where $V=0$ marked on each curve. Areas to the left of the marker are forward biased, and those to the right are reverse biased. The plots coincide with what was seen in fig 4.4. The low diode quality factor of cell A may contribute to the overall shape and smoothness of the curve. N_p is fairly flat for cells B, C, E, and F. Cell D has quite a large amount of uncertainty in the data. Cell B has lower capacitance, which, according to eq. 3.8 coincides with having a large W . For five of the cells, the hole density was in the low-to-mid 10^{16} cm^{-3} range with corresponding depletion widths (W) of 0.3 to 0.4 μm . Cell B, had a much lower hole density (low 10^{15} range) and a value of W near 1 μm . This is not conclusive evidence of having a large depletion region but would coincide with Cell B having low deep penetration losses and the thickest absorber layer.

4.4 Electroluminescence

EL measurements were generally quite uniform. The contact probe can be seen in the middle right area of each cell, or middle bottom of cell D. In each cell there is a recognizable drop-off in applied voltage moving away from the gridlines due to sheet resistance. It is less apparent in poorer performing cells C and E. Defects can be seen in nearly every cell, those on the right hand side of fig 4.6 being more obvious. Cell D which has a stainless steel substrate has defects that span the length of the cell. Cell F has what would appear to be issues with breaks in one gridline in the upper left section of the cell, as does cell A in the center gridline. These breaks may account for significant losses in collection.



Scale in units of $\log_{10}[\text{counts/s}/(\text{mA}/\text{cm}^2)]$

Figure 4.6: Electroluminescence images at $40 \frac{\text{mA}}{\text{cm}^2}$

Note the different intensity scales accompanying each cell. A, B and C are on the same scale, so comparison of those three shows that cell B had a much higher rate of emission than the others due to its relative brightness. It was so much higher that it was imaged for a decade less time because the detector became saturated. Cells D and F are on the same scale and show similar intensity. Cell E's low rate of emission coincides with a low V_{OC} .

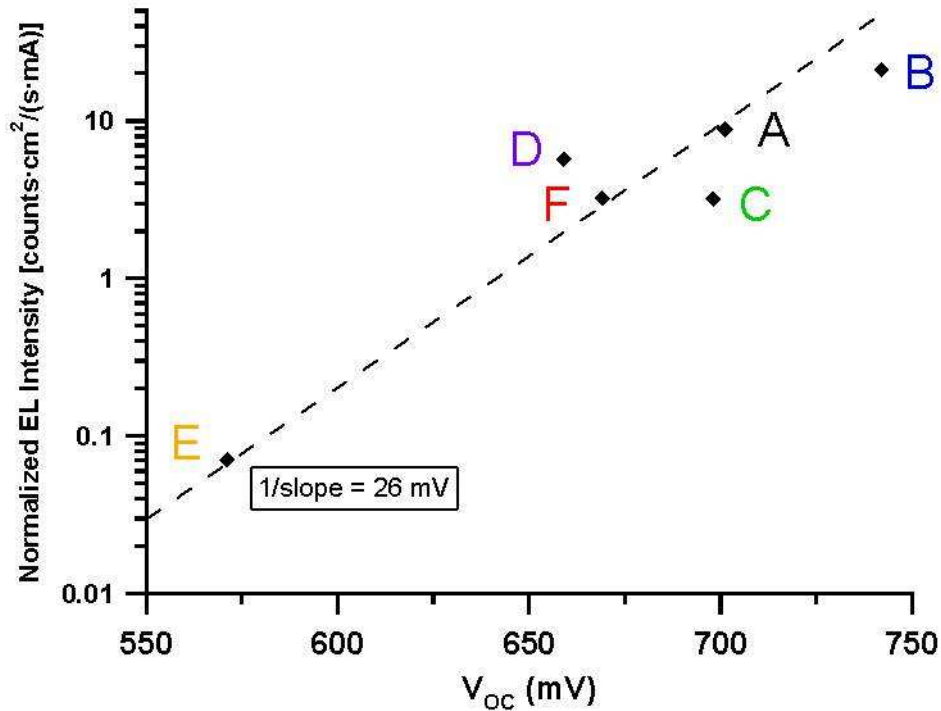


Figure 4.7: Normalized EL vs. V_{OC}

EL has been shown to be exponentially proportional to V_{OC} with slope = q/k_bT [16]. Fig 4.7 shows that the cells in this study generally abide by that relationship with some deviation due to the range of E_g 's found in this study which fall near the detection limits of the CCD camera.

4.5 LBIC

QE measurements revealed that IQE was approximately 99% for each cell at 638 nm and as such LBIC measurements are normalized to this value. Low-resolution LBIC maps are displayed in fig 4.8 in which devices were rastered at a 50- μm step size at 0-V bias with a 100- μm laser spot size.

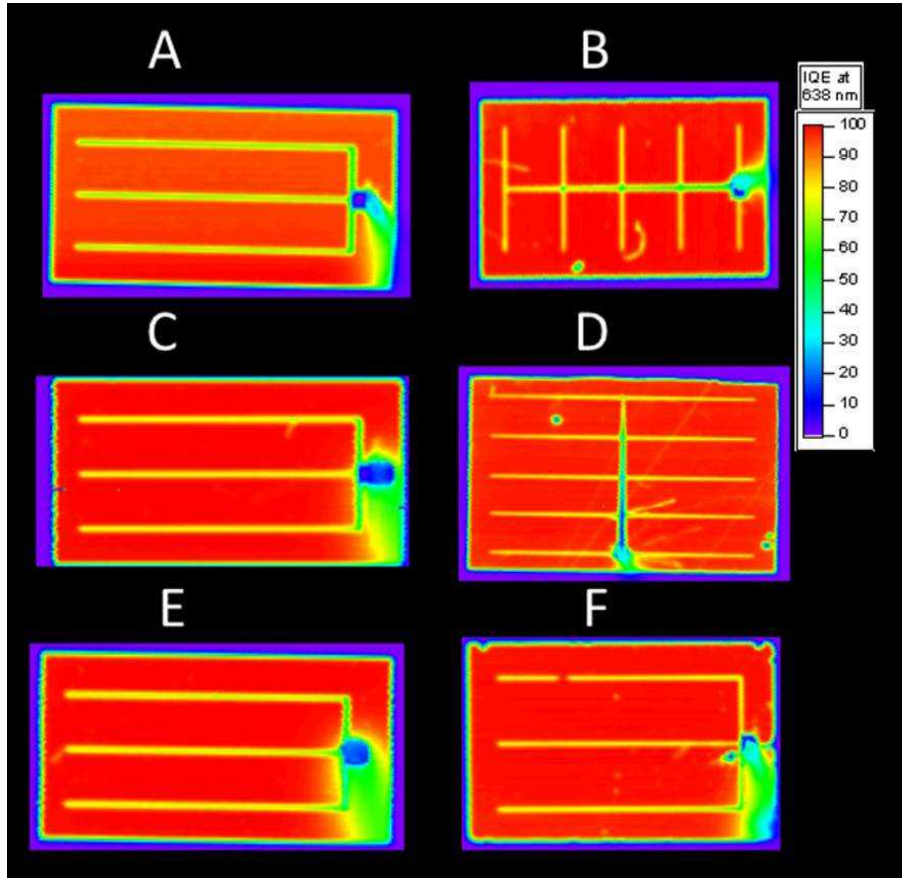


Figure 4.8: LBIC displayed in %QE

LBIC confirms the some of the defects found in EL as well as helps to identify and explain others. The lines on cell D are clear in EL and though faint can be seen in LBIC. Cell B has a curved line in LBIC that does not appear in EL. EL measurements were performed first so there is the possibility of a new scratch due to handling. The grid disconnect in the upper left area of cell F which is clearly shown in EL, is apparent in LBIC, though it seems to be farther to the left hand side. This indicates that there may be another break in the gridline.

4.6 SEM

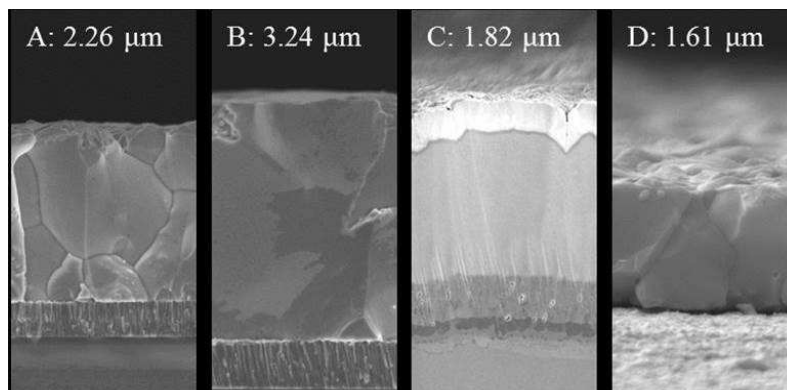


Figure 4.9: SEM images on representative absorber samples from four manufacturers. All images are on the same size scale, and the average absorber thickness measured from each image is as indicated. Compiled by R. Garris

Scanning electron microscopy (SEM) images were collected on representative cells chosen from four of the groups. Results are displayed in fig 4.9. Thickness shown on each image is an average value. Each image is displayed on the same size scale, with the image dimensions being $2.4 \mu\text{m}$ wide and $4.5 \mu\text{m}$ high. Except for sample C the images were collected on bare absorbers prepared by etching the TCO window and buffer layers from finished devices. Samples C and D (those prepared on stainless steel substrates) were prepared for imaging by cutting through the film and were imaged at a small angle. The remaining samples A and B, were prepared by a standard cleave.

The samples deposited by co-evaporation (A,B,D) and co-sputtering (C) show large grain structure, and clean interfaces between the absorber and the Mo. The samples deposited by precursor reaction, and containing sulfur (not shown) show smaller grain size and voids at the interface between the absorber and Mo.

4.7 Auger

Samples were prepared for Auger by etching off the buffer, window and TCO layers. Table 4.3 lists atomic concentrations near the front of the absorber and near the back.

There is no AES profile for sample B (sample containing silver) because high photoconductivity caused a large amount of charging during the measurements and prevented any reasonable data from being obtained.

Table 4.3: Uncorrected atomic concentrations. Concentrations from: Near front→Near back.

Front is 5-10 min avg \sim 50 nm : Back is nearing Mo interface : III=In+Ga, VI=Se+S

Lab	Cu%	In%	Ga%	Se%	S%	Ga/III	S/VI
A	25→26	21→17	6→10	48→47	NA	22→37	NA
C	25→25	17→11	8→13	49→51	NA	32→54	NA
D	27→27	18→13	6→11	49→48	NA	25→54	NA
E	26→25	23→9	3→12	34→31	14→23	11→57	29→42
F	25→24	22→14	2→10	32→38	19→13	8→44	37→34

Fig 4.10 shows Auger profiling for four of the samples used in this project. Cells A and C use the same absorber material but their atomic concentrations are quite different. They both show Cu deficient regions at the surface. The Ga/III ratio in cell C is much higher throughout, which is a likely contributor to higher E_g . Cell D (not pictured) has similar concentrations to cell C. Cells E and F see a larger amount of sulfur at the front and back of the cell, with a smaller S-region in the middle. In all cells we see some In, Ga concentration crossover (the lower concentration becomes the higher concentration) toward the back of the cell. Cell F interestingly has In, Ga, S crossover in the absorber. Cells E and F have an interesting feature in their profiles where several things happen at one point: (1) There is a maxima in sulfur concentration. (2) There is In/Ga crossover. (3) There is a local minimum in selenium content.

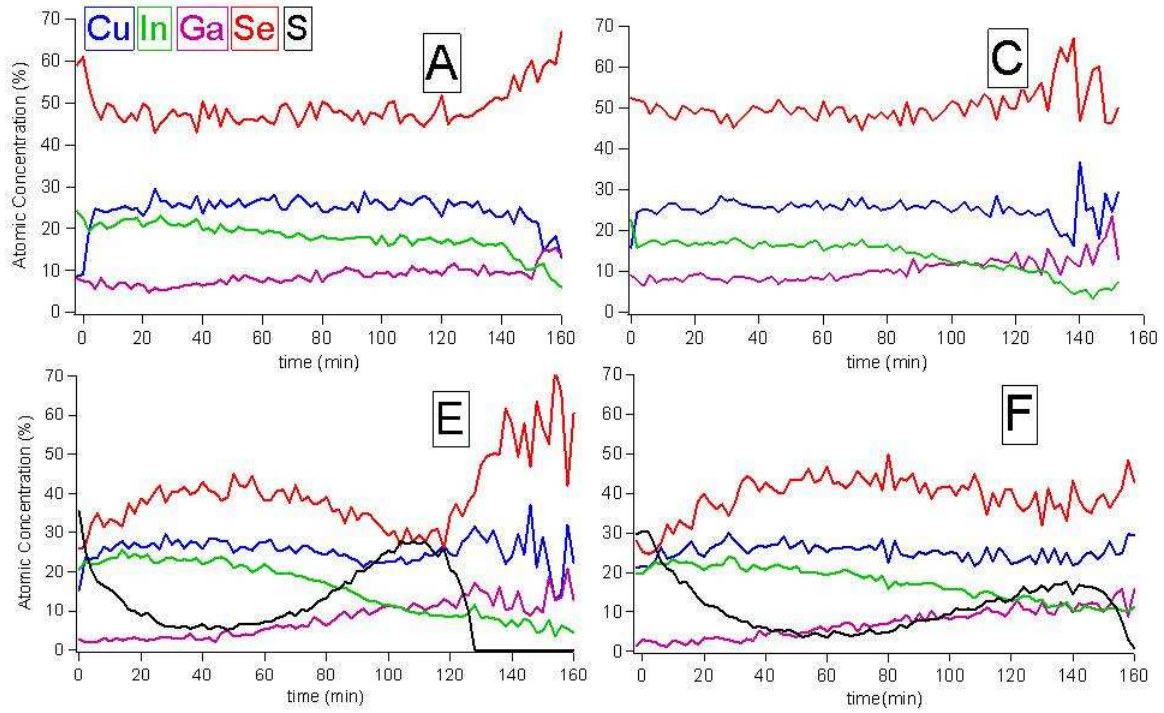


Figure 4.10: Auger atomic profiles

Using Eq 2.1 and Auger elemental concentration data, the bandgap profile can be obtained. These results are displayed in fig 4.11. Bandgap grading in some cases has shown to have a significant effect on cell parameters. There is some degree of grading in each cell, the most obvious being in the cells containing sulfur. It can have the effect of mitigating recombination current J_o in two different ways. Front grading, near the interface, typically involves increasing the band gap through decreasing E_V (fig 2.2). This limits interface recombination and preferentially absorbs blue photons near the front, deeper penetrating red photons are only absorbed further in. Back grading, near the back contact interface typically involves increasing the band gap through increasing E_c . This limits J_o at the back contact [8]. From fig 4.11, cells E and F have front and back E_g grading. Studies have shown sulfur to improve junction quality, and to possibly decrease E_V [17], [18], [19].

Bandgap grading can be informative as to the electrical parameters V_{oc} and J_{sc} . V_{oc} depends strongly on the effective bandgap where photons are absorbed, while J_{sc} is a function of the minimum bandgap. [20]

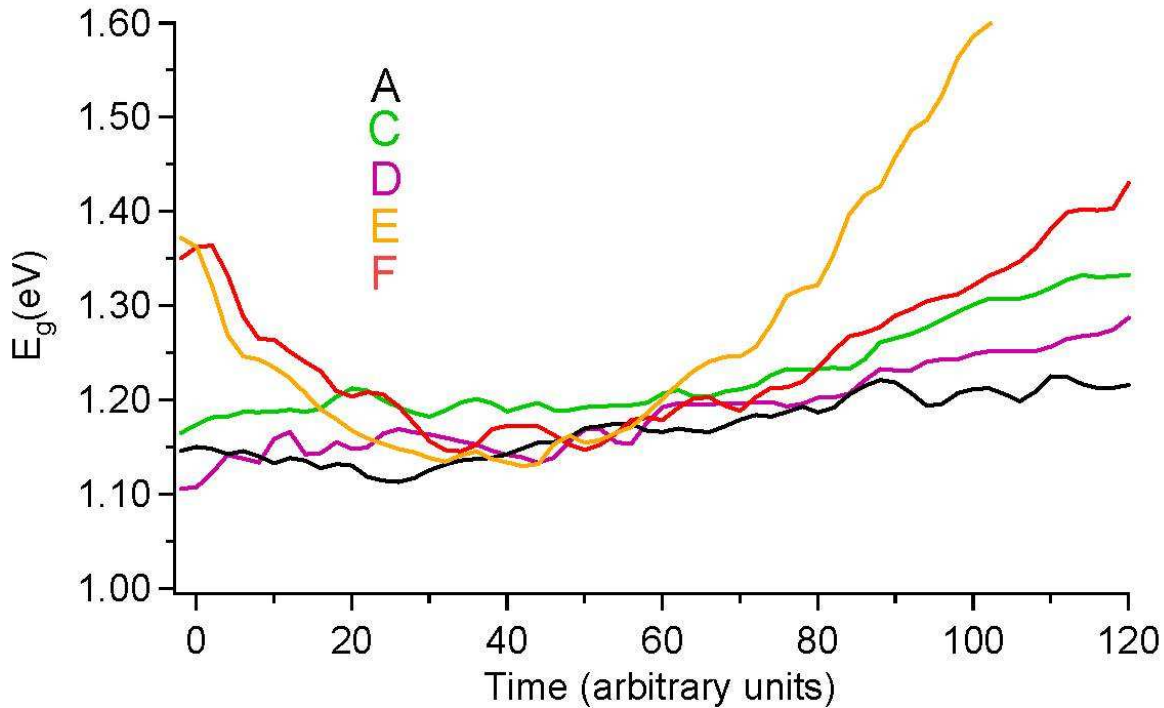


Figure 4.11: Bandgap profiling of cells A,C,D,E, and F. Data are unavailable for lab B. 0 corresponds to the top (sunny side) of the cell. 120 corresponds to reaching the Mo back contact. Here bandgap grading can be seen to different degrees. E_g comes from Eq

Cells A, C, and D employ increasing bandgap toward the back contact. In fact the bandgap of these cells mirror the gradient of the gallium ratios. Cell A has a minimum where the band-gap decreases just past the junction, and then continuously rises toward the back. Cell C shows a graded band-gap that is lower at the front, flat through the middle and then steeply increases toward the back. Cell D shows a nearly uniform gradient from front to back. Cells E and F employ grading at the front and back. The grading in these cells is due to both the gallium and the sulfur content, though it seems to more strongly be a function of sulfur concentration. The band-gap gradient nearly mirrors the sulfur content

in both cells E and F. The gallium content has a constantly increasing slope from front to back. The sulfur content forms a U-shape in cell E. A similar shape is seen in cell F but the slope of the "U" closer to the back has a much gentler slope. A possible conclusion from comparing fig 4.10 and fig 4.11 could be that E and F use sulfur in an attempt to increase the bandgap in the front of the cell and sulfur and gallium to increase the bandgap in the back. Considering this against the typical strategy of bandgap grading described by [8], the data may suggest that sulfur is being used to decrease E_V and Ga is being used to increase E_C . While Auger profiling is informative to the general pattern of grading, it should be noted that there is a large degree of uncertainty due to the different sputtering rates involved with different materials.

Chapter 5

SUMMARY

This purpose of this chapter is to tie together complementary observations, data and inconsistencies. Several trends have become apparent through the course of this study.

Those cells containing sulfur have been able to make high performance cells, with relatively low bandgaps. Through front and back grading, novel TCO materials, and in the case of cell F, through using Zn(O,S) as the buffer layer. The E_g of Zn(O,S) is about 2.8-3.6 eV depending on the oxygen content which is coincident with good transmission of the solar spectrum. Cell F consistently outperformed cell E. Cell F has a lower J_0 , which based on QE measurements, seems to be due at least partially to better mitigation of recombination in the back of the cell. Though cell F performs well it is likely experiencing significant collection losses due to poor gridlines.

A discrepancy that should be noted is found upon comparison of tables 4.1 and 4.2 which shows J_{SC} values from QE and from J-V measurements are not fully consistent. This is to be expected as the two measurements are essentially measuring different things. In J-V the entire device is measured while in QE the monochromatic light is only incident on a small section of the cell, ideally away from gridlines and visible defects. The values measured from QE are higher, which is logical as losses due to grid shading are not accounted for. J_{SC} from J-V will increase by using active area instead of total device area. The exception to the trend of higher J_{SC} from QE is cell D in which the value from QE is lower. QE was performed on several cells from Lab D, and similar low QE values were seen. In both J-V and QE, cell F has the largest value of J_{SC} , and cell C has the lowest value.

It is worth discussing the observed differences in V_{OC} , and the trends by which participants in this study have followed toward attempting to maximize this parameter. A high V_{OC} , is in many cases obtained by having a large doping density [21]. Fig 4.5 shows cells

A,C,D,E, have approximately the same value in low 10^{16} cm^{-3} . Cell B has the lowest doping density of the group; low 10^{15} cm^{-3} . Cell B has a comparatively large depletion region which coincides with the depletion approximation, eq 2.2. IQE and J-V measurements indicate that it has a comparatively low J_{SC} , which is a comparable parameter to J_L . By combining equations 3.3 and 3.5 we can obtain:

$$V_{OC} = \frac{E_g}{q} - \frac{nkT}{q} \cdot \ln \left(\frac{J_{00}}{J_L} \right) \quad (5.1)$$

Cell B has a large value for E_g and a small value for J_0 , both are influential toward a large V_{OC} . The large depletion region improves collection, and the thick absorber region limits recombination toward the back of the cell, decreasing J_{00} . This is evident in IQE, fig 4.3, in which deep penetration losses of cell B are the lowest in the group.

Despite having the same E_g as cell C, cell B has a greater V_{OC} by 50 mV, this may be at least partially due to having a better value for J_0 which may be influenced by the increased absorber thickness (by $\sim 1.4 \mu\text{m}$), and larger depletion region.

Using the same logic, from SEM we saw that cell D has one of the smaller absorber thicknesses, which may relate to the small depletion region seen in C-V, deep penetration losses seen in IQE and a relatively poor value of J_0 . In the same way that cell B has a large V_{OC} a similar conclusion can be drawn as to why cell D should have a relatively small V_{OC} .

Cell B has similar processing to cell A, though it has a larger V_{OC} by 40 mV. Although cell A has a smaller J_0 the larger contributor in eq 5.1 is the difference in E_g .

Cells A and C have similar values of V_{OC} but the lower bandgap of cell A is mitigated by having a much better value for J_0 , (and hence fill-factor) making cell A a much better performer.

Comparison of cells A and D strengthens this argument by showing that though they have a similar bandgap and overall processing, cell A achieves a greater V_{OC} by again having a much smaller J_0 . J-V measurements reveal that cell A has the largest shunting resistance and the highest diode quality factor n , which are indicators of a quality absorber with low recombination.

This analysis points to E_g being the more significant parameter influencing V_{OC} , with J_0 as a good indicator of cell performance.

One aspect that has not been discussed, (because it is unknown) is if the cells deposited on steel have any sodium added to their deposition process. Sodium is known to have several beneficial effects on cell performance that cells deposited on soda-lime glass obtain from the substrate itself [6].

Fig 5.1 is a plot of V_{OC} vs E_g which serves as a helpful diagram of relative cell performance. From eq. 5.1, a large E_g should entail a large V_{OC} and this relationship should be linear with a slope of one. Cells A and B lie on on roughly the same line with slope of one. Cells C, D and E do approximately the same thing. Cell F is an outlier in that it has a large V_{oc} relative to its E_g . As Cell F has the lowest E_g and highest J_{SC} it is likely doing very well with the second term of eq 5.1. One thing that is clear in this study is that there is not a clean relationship between E_g and V_{OC} that is applicable to all the cells in this study.

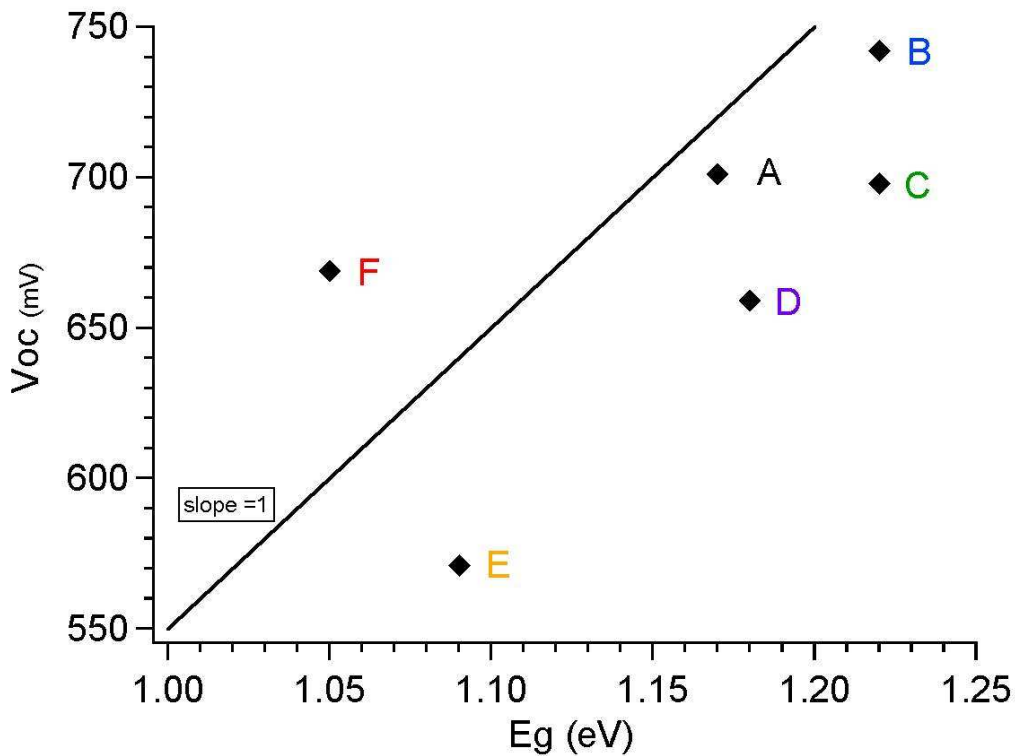


Figure 5.1: V_{OC} vs E_g

This study highlighted specific strengths, similarities, and differences in modern CIGS solar cells. It has been shown that various deposition techniques, and material selections can produce solar cells with significantly different parameters. Several plots in this study demonstrate the wide range of CIGS cells that have high efficiency. The use of sulfur has shown to be beneficial in CIGS cells when used with bandgap grading. Combined with novel TCO materials, high performance solar-cells can be made. Benefits were seen from cells having larger E_g and smaller values of J_0 and n . Each technology leaves ample room for improvement in cell performance. By participating in collaborative projects, the collective knowledge of the field can be reigned in, to the benefit of industry and the scientific community. Overall the study provided a fairly comprehensive look at the state of CIGS solar-cells.

Bibliography

- [1] Kai Maraun and Akane Yamiya. Solar Frontier Achieves World Record Thin-Film Solar Cell Efficiency: 22.3 <http://www.solar-frontier.com/eng/news/2015/C051171.html>, December 2015.
- [2] R.K. Pachauri and L.A. Meyer [eds.]. Climate Change 2014: Synthesis Report. Contribution of Working Groups I, II and III to the Fifth Assessment Report of the Intergovernmental Panel on Climate Change. *Intergovernmental Panel on Climate Change*, 2014.
- [3] Andy Colthorpe. Utility-Scale Solar in the U.S. Now Average 5 Cents per Kilowatt-Hour. internet, October 2015.
- [4] Corey Honeyman. U.S. Solar Market Insight. internet, March 2016.
- [5] Solar Energy Industries Association. Solar Industries Data. online, March 2016.
- [6] William N. Shafarman, Susanne Siebentritt, and Lars Stolt. *Handbook of Photovoltaic Science and Engineering*. John Wiley & Sons, Ltd, 2nd edition, 2011.
- [7] Su-Huai Wei, S.B. Zhang, and Alex Zunger. Effects of Na on the Electrical and Structural Properties of CuInSe_2 . *Journal of Applied Physics*, 85(10):7214–7218, May 1999.
- [8] M. Bar, W. Bohne, J. Rohrich, E. Strub, S. Lindner, M. C. Lux-Steiner, and Ch.-H. Fischer. Determination of the band gap depth profile of the pentenary $\text{Cu}(\text{In}(1-x)\text{Ga}(x))(\text{S}(y)\text{Se}(1-y))_2$ chalcopyrite from its composition gradient. *Journal of Applied Physics*, 96(7):3857–3860, October 2004.
- [9] S.M. Sze and Kwok K. Ng. *Physics of Semiconductor Devices*. Wiley-interscience, 2007.
- [10] Markus Gloeckler. *Device Physics of $\text{Cu}(\text{In},\text{Ga})\text{Se}_2$ Thin-Film Solar Cells*. PhD thesis, Colorado State University, 2005.

- [11] Roland Scheer and Hans Werner Schock. *Chalcogenide Photovoltaics Physics, Technologies and Thin Film Devices*. WILEY-VCH, 2011.
- [12] Steven S. Hegedus and William Shafarman. Thin-Film Solar Cells: Device Measurements and Analysis. *Progress in Photovoltaics: Research and Applications*, 12:155–176, March 2004.
- [13] Russell M. Geisthardt. *Device Characterization of Cadmium Telluride Photovoltaics*. PhD thesis, Colorado State University, 2014.
- [14] Jennifer Heath and Pawel Zabierowski. *Advanced Characterization Techniques for Thin Film Solar Cells*. Wiley-Vch, 2011.
- [15] T. Kirchartz, U. Rau, M. Kurth, J. Mattheis, and J.H. Werner. Comparative study of electroluminescence from Cu(In,Ga)Se₂ and Si Solar cells. *Thin Solid Films*, pages 6238–6242, January 2007.
- [16] J.M. Raguse and J.R. Sites. Correlation of Electroluminescence With Open-Circuit Voltage From Thin-Film CdTe Solar Cells. *IEEE Journal of Photovoltaics*, 5(4):1175–1178, July 2015.
- [17] Udai P. Singh, William N. Shafarman, and Robert W. Birkmire. Surface sulfurization studies of Cu(InGa)Se₂ Thin Film. *Solar Energy Materials and Solar Cells*, 90(5):623 – 630, June 2006.
- [18] Ishwor Khatri, Isamu Matsuyama, Hiroshi Yamaguchi, Hirofumi Fukai, and Tokio Nakada. Surface Sulfurization on MBE-grown Cu(In_{1-x},Ga_x)Se₂ Thin Films and Devices. *Japanese Journal of Applied Physics*, 54(8S1):08KC10, March 2015.
- [19] Yoshinori Nagoya, Katsumi Kushiya, Muneyori Tachiyuki, and Osamu Yamase. Role of Incorporated Sulfur Into the Surface of Cu(InGa)Se₂ Thin-Film Absorber. *Solar Energy Materials and Solar Cells*, 67(14):247 – 253, March 2001. {PVSEC} 11 - {PART} {III}.

- [20] I.L. Repins, B.J. Stanberry, D.L. Young, S.S. Li, W.K. Metzger, C.L. Perkins, W.N. Shafarman, M.E. Beck and L. Chen and V.K. kapur, D. Tarrant, M.D. Gonzalez, D.G. Jensen, T.J. Anderson, W. Wang and L.L. Kerr, B. Keys, S. Asher, A. Delahoy, and B. Von Roedern. Comparison of Device Performance and Measured Transport Parameters in Widely-Varying Cu(In,Ga)(Se,S) Solar Cells. *Progress in Photovoltaics: Research and Applications*, 14:25–43, October 2006.
- [21] Christiana Honsberg and Stuart Bowden. pveducation.org. internet, March 2016.